MONTAN UNIVERSITÄT

Final Report

Mechanical Testing and Failure Analysis of Miniaturized Functional Ceramic Components

Johannes Neumüller

Supervisors MUL:

Univ. Prof. Dr. Raul Bermejo &

Ao. Univ. Prof. Dr. Peter Supancic

Supervisor PSU:

Prof. Dr. Susan Trolier-McKinstry

Austrian Marshall Plan Foundation

PennState College of Earth and Mineral Sciences | Department of Materials Science and Engineering

Abstract

In this study, various test setups were developed to apply a controlled mechanical load on functional ceramic components. For this purpose, a setup for static biaxial testing of coatings on silicon samples under elevated humidity and temperature was implemented. The setup was tested with a coating consisting of a thin ALD layer and an organic topcoat. The strength evaluation was carried out using a specially developed Python library based on the standardized maximum likelihood approach. In addition, a setup with dynamic load application was set up and tested on the same coating. No cracks or other defects were found within the load range available through the substrate.

Additionally, a setup for mechanical loading of multilayer ceramic capacitors (MLCCs) was established. This setup was tested on commercial MLCCs afterwards. No defects were found in the mechanically loaded components during the electrical characterization of the components.

Table of Contents

1. Introduction

Functional ceramics possess unique properties that are inherent to the material itself. These properties can be used for the fabrication of various electrical components, such as multilayer ceramic capacitors (MLCCs) or electromechanical components like piezoelectric actuators and microelectromechanical systems (MEMS). Both types of systems face challenges due to thermal and mechanical stresses encountered during their operational lifespan, which can result in failures.

In the case of piezoelectric actuators, a humid environment is known to increase failure. Electrochemical degradation can occur after a short period of time. In the case of thin-film actuators, the influence of different electrodes on this effect has already been investigated. It appears that moisture leads to the failure of the components regardless of the electrode materials used. [1]

A common method to prevent moisture contact in bulk actuators is to seal them in a steel housing. This is associated with high costs and is not applicable to thin-film piezo components. A coating that is already being tested for implantable electronics could provide a solution. It involves a combination of an inorganic atomic layer deposition (ALD) coating with an organic Parylene C coating. [2]

These coatings could be applied to both bulk piezo stacks and thin films without compromising their functionality. It is necessary to test their mechanical properties to ensure their suitability for this application, particularly regarding the maximum strain they can withstand without failing.

To test the coating itself, it was applied to a silicon substrate. This made it possible to mechanically test the coating by applying an external load.

For this purpose, a test setup has been developed which enables the biaxial mechanical testing of coatings on a silicon substrate under various conditions. These conditions include static testing under increased humidity and elevated temperature, as well as dynamic testing.

In the case of multilayer ceramic capacitors, stresses arising during manufacturing and assembly processes can be particularly problematic. In this context, it is particularly important to detect damage prior to the deployment of the component in a system to prevent system failure.

Crack or defect detection can be done by methods like X-ray imaging or also using acoustic phenomena like ultrasonic imaging afterwards. [3] [4]

To reliably verify these characterization methods, it is necessary to intentionally introduce defects. In this regard, the potential damage caused by manual soldering of MLCCs has already been investigated through various thermal shock experiments. [5]

A methodology to apply a mechanical stress after mounting the MLCC device on a PCB is also established. In this case a specified strain is applied to the printed circuit board (PCB) which can lead to cracks. [3]

Another method to mechanically test these components is the 3-point bending test. Due to the small geometries of the components, it is necessary to use a special support fixture. This allows for a very defined mechanical stress field to be applied. This test and the possibility of a local thermal shock test will be further investigated in this study.

2. Testing methods

A variety of test methods are available for determining the strength of ceramic materials. For the moisture protection coatings project, it is necessary to achieve the highest possible strength of the substrate in order to expose the coating to the greatest possible load. For this reason, square samples were used, which are suitable for the biaxial ball on three balls test. This can minimize failure of the samples due to edge defects by reducing the stress at the edge.

For the MLCC project, a biaxial test method would also be preferable in order to minimize failure due to edge defects. Here it was not possible to obtain suitable components within the residence time. Therefore, the three-point bending test was used, which is also applicable for more common MLCCs.

2.1. Ball-on-three-balls-test (B3B-test)

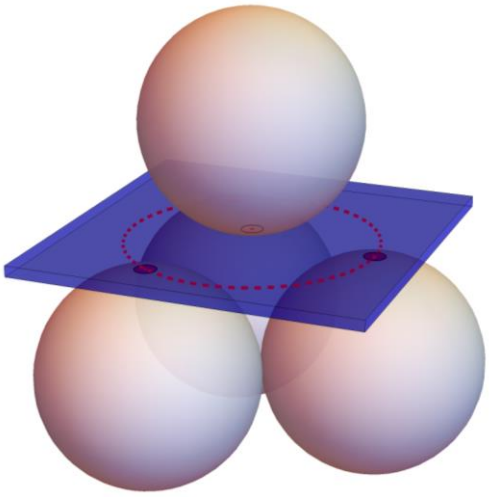

Figure 1: Schematic of the Ball on three balls setup.

Figure 2: Picture of the used ball on three balls setup.

In the ball on three balls test (B3B test), the sample under examination is supported by three touching spheres and loaded with a fourth sphere at the center of the opposite side. Figure 1 schematically illustrates this situation. In the B3B test, the maximum stress occurs at the center of the sample. The stress at the edge is significantly lower, thereby minimizing the probability of failure due to an edge defect. The B3B test is tolerant of minor non-planarities, which do not occur in wafer samples anyway. Nevertheless, the friction with the substrate is lower compared to the ring-on-ring test, which has a positive effect on the measurements. Figure 2 shows the experimental setup for ambient conditions which was used in this study.

The main drawback of this testing method is the associated complex analysis of the experiments. Currently, an exact analytical description of the stress field is not possible, necessitating a numerical solution using the Finite Element Method. [6] [7] A recent approximation solution for isotropic elastic materials has been published, which adequately approximates this factor with the existing geometry with sufficient accuracy. [8]

The following relationship is used to calculate the maximal applied stress of a sample:

$$\sigma = f \frac{F}{t^2} \tag{1}$$

f denotes the proportionality factor, which describes the influence of the test conditions. It depends on the specimen and support geometry, as well as on the material parameters of the specimen and support balls. [8] This factor is determined using the following approximation formulas. *F* is the measured force and *t* corresponds to the specimen thickness.

$$f = f_{new}\, k_1\, k_2 \tag{2}$$

The proportionality factor consists of three terms. f_{new} is an empirical fit factor. k_1 and k_2 are additional factors which improve the accuracy for high-load testing conditions.

Table 1: Constants m_1 - m_3 utilized in equation (3)

m_1	m_2	m_3
0.697	-0.118	-0.728

The f_{new} factor can be determined by

$$f_{new}\left(\frac{t}{R_s}, \frac{R}{R_s}, \nu\right) = \exp\left[m_1(1+\nu) + m_2 \ln\frac{t}{R_s} + m_3 \sqrt[4]{\frac{R\, t^2}{R_s^3}}\right] \tag{3}$$

where the support radius R_s is determined by

$$R_s = R_{LB}\frac{2}{\sqrt{3}} \tag{4}$$

R_{LB} is the load ball radius. The radius of the sample R corresponds to the half of the effective diameter D_{eff}, which is calculated by

$$R = \frac{1}{2}D_{eff} = \frac{L}{2}\left(1.053 - 0.017\frac{t\, L}{R_s^2}\right) \tag{5}$$

L is hereby the length of the squared sample

The effective diameter is necessary because square samples were used instead of discs.

The fitting constants to evaluate equation (*3*) are given in Table 1.

Table 2: Constants h_1 - h_5 utilized in equation (6)

h_1	h_2	h_3	h_4	h_5
1.0052	0.00063	-0.5928	1.6756	1.3523

The first fitting parameter k_1 can be determined by

$$k_1\left(\frac{R_c}{R_s}, \frac{t}{R_s}, \nu, E, E_{LB}, \nu_{LB}, F\right) = h_1 + h_2 \ln\left(\frac{R_c}{R_s}\,\frac{t}{R_s}\right) + h_3\frac{(R_c/R_s)^{h_4}}{(t/R_s)^{h_5}} \tag{6}$$

Where R_c is the contact radius based on the Hertzian solution and can be determined by

$$R_C = \sqrt[3]{\frac{3\, F\, R_{LB}}{4}\left(\frac{1-\nu^2}{E} + \frac{1-\nu_{LB}^2}{E_{LB}}\right)} \tag{7}$$

With the Poisson's ratio of the sample ν, and the Young's modulus of the sample E. ν_{LB} is the Poisson's ratio of the loading ball and E_{LB} the corresponding Young's modulus.

The second fitting parameter can be calculated with the following formula:

$$k_2 = 1 + \frac{\sqrt{3}}{2}\frac{F}{E\, t^2}\left[(1-\nu^2)\frac{R/R_s}{t/R_s}\left(0.0015 - 1.13\frac{1}{(R/R_s)^2}\right)\right] \tag{8}$$

2.2. Three-point-bending-test

Another method of determining the strength of ceramics is the bending test. Especially for small samples the three-point-bending test is more suitable. Therefore, this testing method was used for testing the MLCCs. A miniaturized testing fixture was created to test the small samples. It is capable for samples with an 1812 case size.

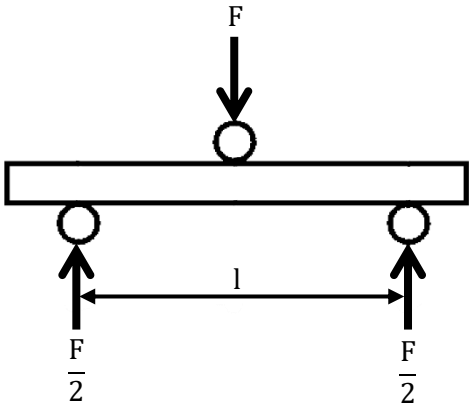

Figure 3: Schematic of the 3-point-bending-test.

Figure 4: Picture of the used 3-point-bending setup.

For the calculation of the maximum stress σ which occurs at the surface on the opposing side where the upper roller is in contact with the sample, the following formula was used, based on Bernoulli's beam theory. [9]

$$\sigma = \frac{3\,F\,l}{2\,w\,t^2} \tag{9}$$

Where F is the maximum force, l the support distance between the lower rollers, w the sample width and t the sample thickness.

3. Weibull analysis

3.1. Weibull theory

The strength of ceramics and other brittle materials (glasses, glass-ceramics, semiconducting and dielectric wafer-materials) generally exhibits significant scatter. This is attributed to the distribution of size and position of defects contained within them, as the failure of ceramics originates from flaws within the material. These flaws can be both volume and surface defects. One approach to describing this strength behaviour is the Weibull theory, attributed to the work of Weibull [10]. The application of this theory assumes that failure arises from a single type of defect. To enable the description of heterogeneous stress distributions, the use of the effective volume is necessary. When comparing only test series with the same sample geometry, it is possible to equate the effective volume with the reference volume related to the characteristic strength, thereby eliminating the need to calculate the effective volume. The probability of failure F for a stress σ under these assumptions can be defined as follows [11]:

$$F(V_{eff},\sigma) = 1 - \exp\left[-\frac{V_{eff}}{V_0}\left(\frac{\sigma}{\sigma_0}\right)^m\right] \quad (10)$$

V_0 refers to the reference volume, σ_0 is the corresponding characteristic strength and m is the Weibull modulus.

By choosing the reference volume V_0 as the actual effective volume V_{eff} these terms cancel and the equation simplifies to the following formula

$$F(\sigma) = 1 - \exp\left[-\left(\frac{\sigma}{\sigma_0}\right)^m\right] \quad (11)$$

3.2. Determination of the Weibull parameters

One method for determining the characteristic strength σ_0 and the estimated Weibull modulus is the Maximum Likelihood Method. In this method, m is numerically determined from equation (12) Subsequently, the characteristic strength can be calculated using formula (13). [12]

$$\frac{\sum_{j=1}^{N}\left[ln(\sigma_{f,j}) * {\sigma_{f,j}}^m\right]}{\sum_{j=1}^{N}{\sigma_{f,j}}^m} - \frac{1}{N}\sum_{j=1}^{N} ln(\sigma_{f,j}) - \frac{1}{m} = 0 \quad (12)$$

$$\sigma_0 = \left[\left(\sum_{j=1}^{N}{\sigma_{f,j}}^m\right)\frac{1}{N}\right]^{1/m} \quad (13)$$

N denotes the number of samples and σ_{fj} the measured strength of each respective sample. Through this method, m is consistently overestimated, which is why a correction factor b must be considered. The corresponding value for this can be obtained from the standard [12]. m_{corr} denotes the corrected Weibull modulus.

$$m_{cor} = m * b \quad (14)$$

The systematic deviation of the characteristic strength is significantly lower compared to that of the Weibull modulus, hence no correction is necessary for it.

3.3. Weibull diagram

For visualization of the Weibull distribution, the Weibull plot is used, which corresponds to a linearized representation of equation (10). The reference volume V_0 can be equated to the effective volume V_{eff}, as long as all samples have the same geometry and are tested with the same setup. (Equation (11)). Initially, the strength data are arranged in ascending order. Each data point is assigned an estimated value for the probability of failure using equation (15).

$$P_{f,i} = \frac{i - 0{,}5}{N} \quad (15)$$

Equation (16) is used to calculate the ordinate values of the diagram.

$$y_i = ln\left[ln\left(\frac{1}{1 - P_{f,i}}\right)\right] \quad (16)$$

Equation (17) is used to calculate the abscissa values.

$$x_i = ln(\sigma_{f,i}) \quad (17)$$

3.4. Python library for evaluation

To automate the evaluation, a library was programmed. Python was chosen as the programming language for this purpose, because it is an open-source software, allowing the library to be used without the need for paid licenses. The library is suitable for the B3B test and the 3-point bending test. Initially, it reads the raw data from the machine, which includes force, displacement data, and their corresponding timestamps. From these, the maximum force can be determined, which corresponds to the fracture force. Depending on the test used, the fracture stress is then determined. For the ball-on-three-balls test, the f-factor is determined using the previously described approximation formula. For the 3-point bending test, the corresponding analytical formula is used. The 4-point bending test has also been implemented, although it is not discussed here in detail. Due to the modular programming, it is relatively easy to implement other tests for determining the strength of ceramics, such as the ring-on-ring test.

The Weibull analysis is performed according to the standard [12]. The respective formulas are given in the section about the determination of the Weibull parameters. The 90% confidence intervals for the Weibull parameters are also determined. To use the library, it is best to import it into a Jupyter notebook and then call the function for the Weibull analysis. An example of this is shown in Figure 5. Afterwards, the calculated Weibull parameters, including their confidence intervals, can be outputted using the print function. It is also possible to analyse a variety of test series together. To do this, the directory containing the data must be specified.

```
In [1]: # Import library for evaluation and plotting library
        import Weibull_evaluation
        import matplotlib.pyplot as plt

In [2]: # Define measurement_properties:
        properties = Weibull_evaluation.Properties_B3B(sample_length=12,sample_thickness=0.38,
                                                       ball_radius=7.5/2,poissons_ratio=0.3,
                                                       e_modulus=126000)

In [3]: # Load raw data and determine Weibull parameter
        weibull_data=Weibull_evaluation.WeibullAnalysisData.generate_weibull_analysis_data_from_measurement_data(
            path_to_measurement_files="ambient_conditions_strength_analysis", name="ambient_conditions_strength_analysis",
            measurement_properties=properties)

In [4]: # Print Weibull-parameter
        print(weibull_data)

        Name: ambient_conditions_strength_analysis
        Number of samples: 15
        Characteristic strength: 1923 [1866 - 1984] MPa
        Weibull modulus: 15 [11 - 21]
```

Figure 5: Exemplary code to do the Weibull analysis with the Python library.

It is also possible to plot Weibull diagrams using this library. The confidence intervals can optionally be displayed as well. A custom axis has been created for the vertical axis, directly showing the probability of failure. This significantly facilitates the interpretation of Weibull plots. Figure 6 shows a code example for creating a Weibull diagram.

```
In [5]: Weibull_evaluation.plot_weibull_diagram(weibull_data,show_confidence_intervals=True,colors_list='#e6194b',x_limit_low=1000,
                                                x_limit_high=3000,x_ticks_starting_value=1000,x_major_ticks_interval=500,
                                                x_minor_ticks_interval=250,show_legend=False)
        plt.show()
```

Figure 6: Exemplary code to create a Weibull diagram.

4. Development of the testing setup for the moisture barrier coatings

4.1. Investigation of the substrate

A strength analysis of the uncoated substrate was carried out to estimate the loads the substrate could withstand. These were tested at ambient conditions with a target time to failure between 2 - 5 seconds to determine the inert strength. The ball-on-three-ball setup on an MTS Criterion 43 press machine with a 1 kN load cell was used for the measurement. A test rate of 3 mm/min was used. The preload was set to 10 N.

Figure 7: Picture of the Si-sample.

A single crystalline Si wafer (orientation: <001>) with a diameter of 3 inch and a thickness of 380 µm with a 70 nm thermal oxide layer was used as the substrate material. The wafer was diced into 12 x 12 mm² square samples where the axes were aligned along the basic cubic crystallographic axes. For this measurement, 15 samples were used to keep the confidence intervals small enough to estimate the strength distribution.

Stainless steel balls were used for the test, which is why a Young's modulus for the loading balls E_{LB} of 210 000 MPa and a Poisson's ratio ν_{LB} of 0.33 were assumed. For the strength and strain evaluation equivalent elastic constants have been chosen according [13]. 126 000 MPa was used for the Young's modulus of the samples E and a Poisson's ratio of 0.3. The Young's modulus results from a biaxial modulus M of 180 000 MPa [14] used in equation (18).

$$E = M\,(1-\nu) \tag{18}$$

The stress was determined based on equation (1).

Hooke's law (19) was applied to obtain an estimate of the biaxial failure surface strain corresponding to the strain at the coating.

$$\varepsilon = \frac{\sigma\,(1-\nu)}{E} = \frac{\sigma}{M} \tag{19}$$

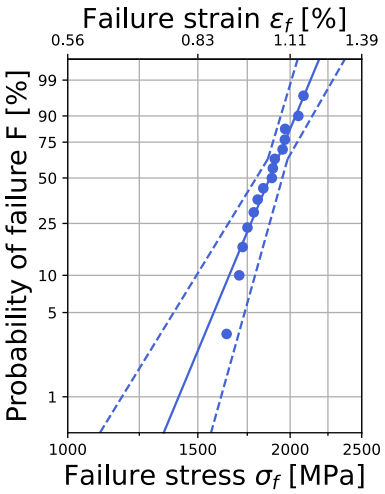

Figure 8: Weibull diagram of the uncoated Si-substrate.

Figure 8 shows the corresponding Weibull diagram of the measurement. The resulting characteristic strength σ_0 is 1923 [1866 – 1924] MPa and the Weibull modulus is 15 [11 – 21]. The 90% confidence intervals are given in square brackets. The failure strain, which was calculated according to equation (19) is plotted on a second horizontal axis, to get an estimation of the surface strain which corresponds to the strain at the coating afterwards.

By inserting equation (1) into equation (19), the force required for different strains can be calculated. This requires a numerical solver, as the proportionality factor f also depends on the force F.

Equation (11) and equation (19) were used to estimate the probability of failure.

Table 3: Estimated probability of failure for different strains

ε [%]	σ [MPa]	Load [N]	F [%]
0.3	540	31.2	0.0
0.4	720	41.9	0.0
0.5	900	52.9	0.0
0.6	1080	64.0	0.0
0.7	1260	75.4	0.2
0.8	1440	86.9	1.3
0.9	1620	98.6	7.4
1.0	1800	110.5	31.1
1.1	1980	122.6	78.6
1.2	2160	134.9	99.7

Table 3 shows the estimated probability of failure for different strains and their corresponding stress and load. Strains of up to 0.9 % seem to be applicable without a high failure probability.

This measured data was compared to literature values with a similar substrate. [15]

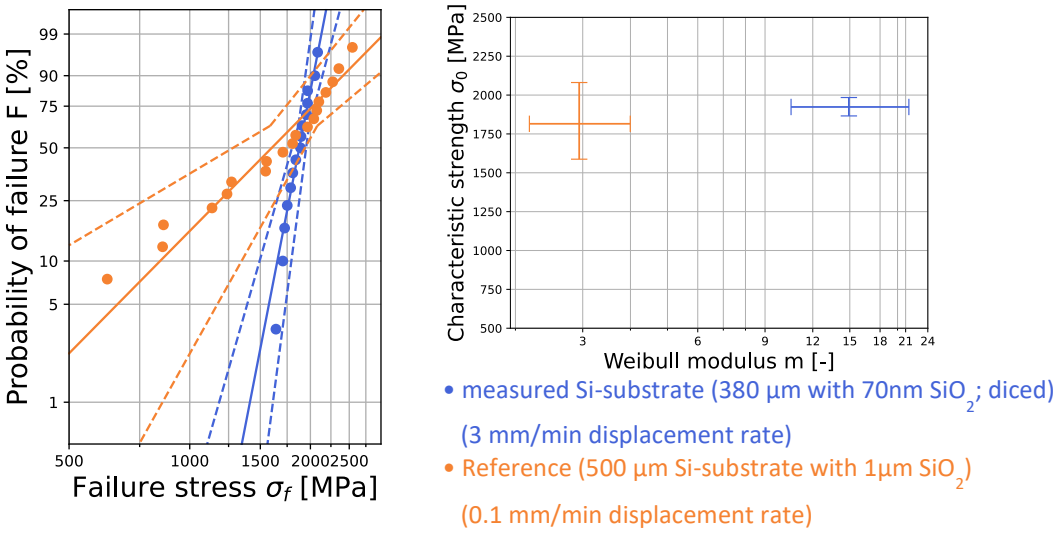

Figure 9: Weibull diagram and σ0 – m diagram of uncoated substrate and reference series.

Figure 9 shows the Weibull diagram and the characteristic strength in relation to the Weibull modulus. The 90% confidence intervals of the characteristic strength of both series are overlapping, but the Weibull modulus has a significant difference. One possible reason for this difference could be the different sample preparation. One series was diced, the other cleaved. This can lead to a different distribution of defects in the edge area. If the samples fail from the edge, this can lead to a different strength distribution.

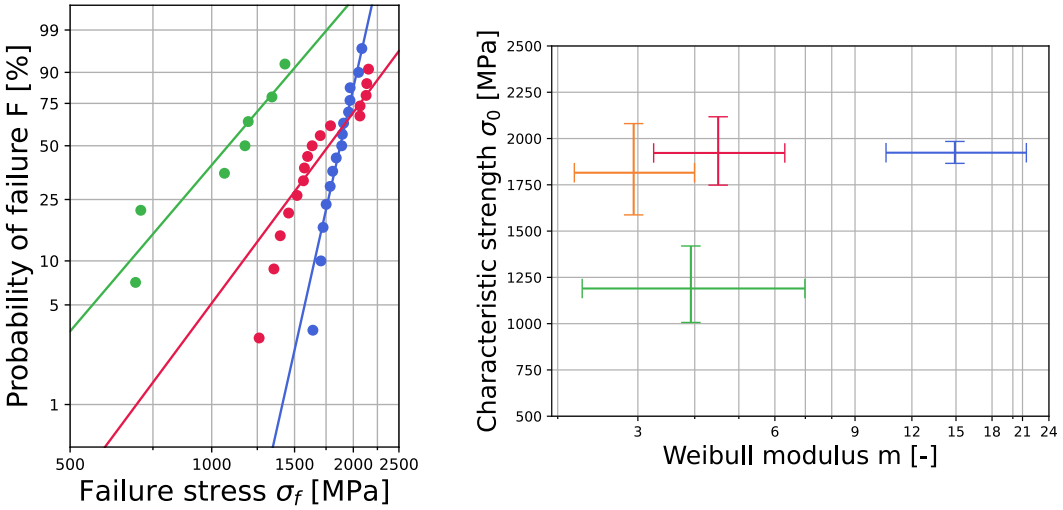

• diced Si-substrate (380 µm with 70nm SiO_2)
• cleaved Si-substrate (380 µm with 70nm SiO_2)
• cleaved coated samples (ALD: 15 nm Al_2O_3 and 5 nm TiO_2)
• Reference (500 µm Si-substrate with 1µm SiO_2)

Figure 10: Weibull diagram and σ_0 – m diagram to compare cleaved and diced samples.

Figure 10 makes a comparison between different sample processing methods. Additionally cleaved coated samples are shown, in order to show the importance of the sample preparation. The uncoated samples have no significant difference in the characteristic strength. Just the Weibull modulus of the diced samples is higher compared to the cleaved samples. The series of coated samples also has a significant lower characteristic strength.

In most cases, the failure of ceramics is attributed to the unstable propagation of defects, which are formed during manufacturing or surface treatment. These include cracks, pores, inclusions, as well as scratches. Linear elastic fracture mechanics deals with the propagation of cracks and at which stress level they become critical, subsequently causing fracture. [11]

Using Equation (20), the stress intensity factor K_I can be calculated from the applied stress σ, a geometric factor Y, and the effective defect size a.

$$K_I = \sigma\, Y \sqrt{\pi\, a} \tag{20}$$

Once the critical stress intensity K_{IC} is reached, unstable crack propagation occurs, leading to sample failure. In this case, σ corresponds to the fracture stress σ_f and a to the critical defect size a_c. This relationship is shown below:

$$K_{Ic} = \sigma_f\, Y \sqrt{\pi\, a_c} \tag{21}$$

If the critical stress intensity is known and a specific type of defect is assumed, the critical defect size can be approximately determined. This is possible through the rearrangement of Equation (21) resulting in the following formula:

$$a_c = \frac{{K_{Ic}}^2}{\pi\, {\sigma_f}^2 Y^2} \tag{22}$$

For the critical stress intensity of <100> silicon, a value of 0.73 $\mathrm{MPa}\sqrt{\mathrm{m}}$ was assumed. [13] A geometric factor of 1.12 was used, assuming surface defects. [16] The failure origin was assumed to be in the center of the tensile loaded surface, and not at the edges. Consequently, the defect size distribution of the three series was determined, as shown in Figure 11.

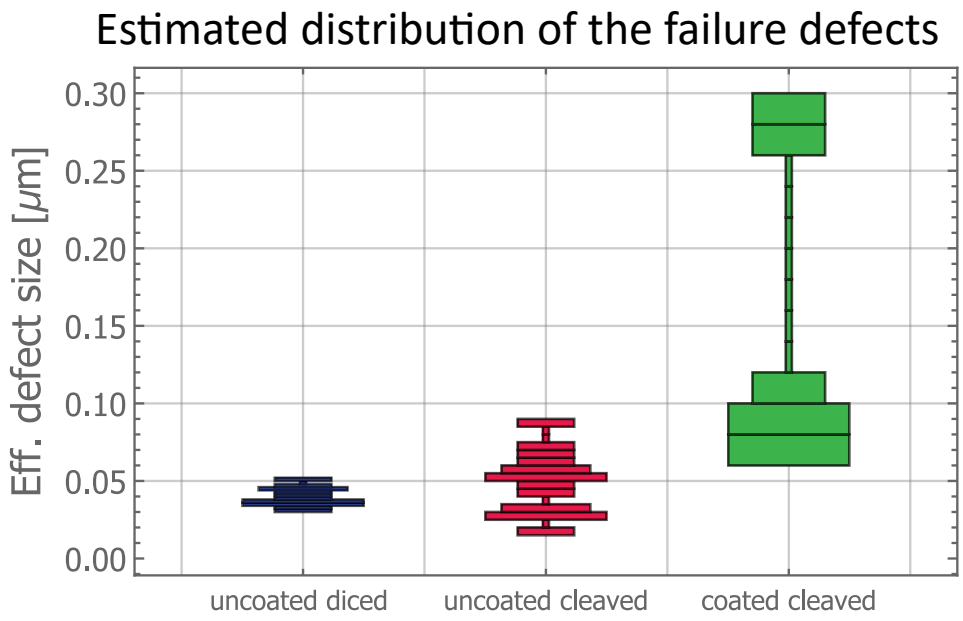

Figure 11: Diagram for estimated distribution of failure defects.

It is apparent that significantly larger defects occurred in the coated samples. Since these defects are much larger than the coating itself, it can be inferred that additional defects were introduced during the cleaning process prior to coating. This showed that sample preparation plays an important role and that even very small defects can lead to a significant reduction in substrate strength.

4.2. Testing at elevated humidity

A sealable bag was placed around the panels to create a test environment with increased humidity. A saturated sodium chloride (NaCl) solution was placed together with the B3B fixture inside the bag. An Arduino microcontroller (Arduino Nano 33 BLE) with an integrated humidity sensor was used to measure the relative humidity and with a Python script the data was logged and stored afterwards. With a small fan on top of the NaCl-solution container the process of creating a constant humidity level was accelerated.

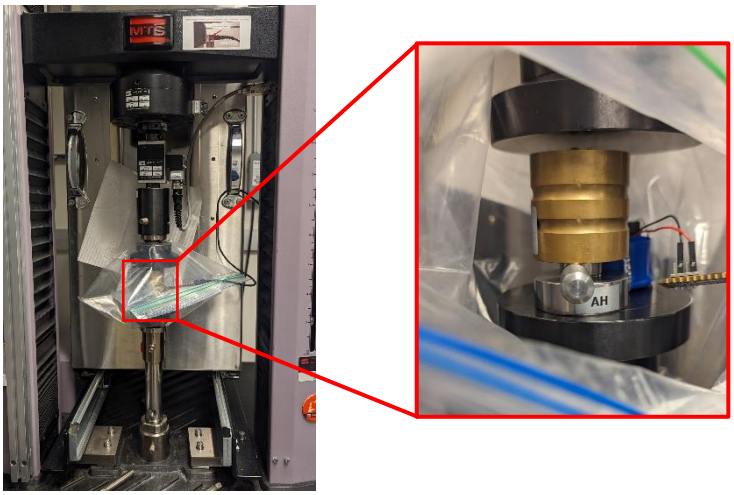

Figure 12: Picture of the setup for B3B-testing at elevated humidity.

The saturation level of the solution was at about 70% relative humidity. This level was reached within a few minutes after closing the bag. After applying the preload, the pin has to be removed. This also led to a drop in the humidity value, even when the bag stayed closed. The reason for this is probably the sensitivity of the air flow sensor.

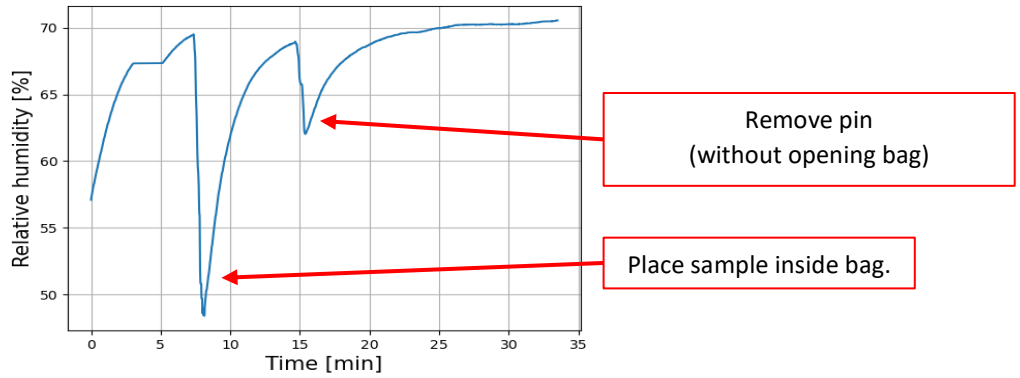

Figure 13: Exemplar humidity curve measured during test at elevated humidity.

4.2.1. Investigation of subcritical crack growth of the substrate

In many ceramic materials, subcritical crack growth occurs, often leading to failure of specimens below the critical stress intensity, particularly under the influence of increased humidity, resulting in decreased strength. [17] [18] The material was tested for subcritical crack growth to ensure that the strength distribution of the Si substrate does not change with increased humidity. For this purpose, a series of tests were conducted on uncoated samples under increased humidity at a significantly slower displacement rate. This was intended to accentuate subcritical crack growth if present in the material.

The time to failure was extended from the 2 - 5 seconds observed in tests conducted under ambient conditions to 85 - 120 seconds. A relative humidity of approximately 70% was measured.

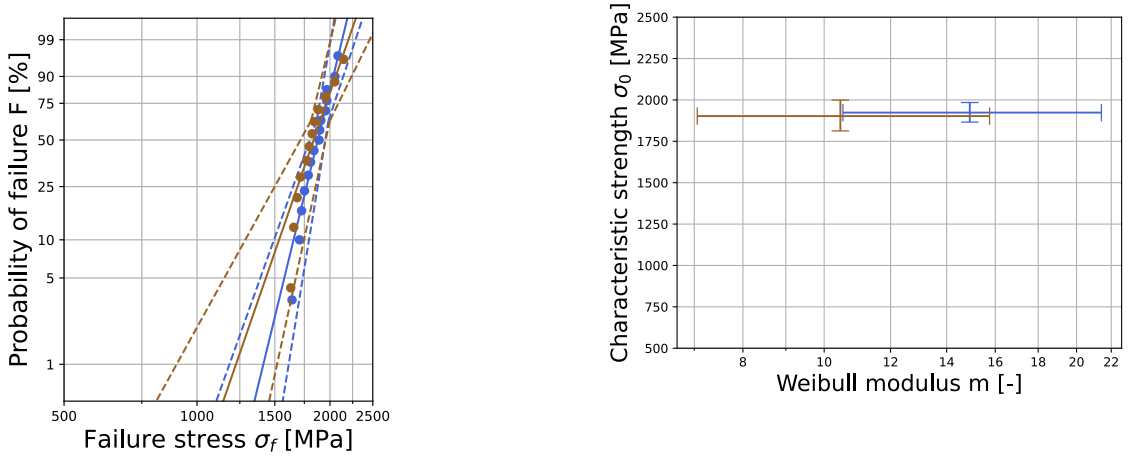

- Si-substrate ambient conditions with high testing speed (v = 3 mm/min → time to failure: 2 - 5 s)
- Si-substrate ≈ 70% RH ambient temperature with low testing speed (v=0.1mm/min → time to failure: 85 - 120 s)

Figure 14: Weibull diagram and σ_0- m diagram of Si-substrate tested at ambient conditions and elevated humidity.

Figure 14 shows the corresponding Weibull diagram and the σ_0- m diagram. It is evident that both the characteristic strength and the Weibull modulus are not significantly different, as the 90% confidence intervals consistently overlap. Thus, it is apparent that no change in the strength distribution can be expected under mechanical loading of the substrate at increased humidity, allowing for the continued use of the previously determined Weibull distribution.

4.3. Testing at elevated temperatures

Figure 15: B3B testing setup including the temperature chamber for testing at elevated temperature.

For the testing at elevated temperatures a temperature chamber (MTS Advantage Environmental Chamber) was included in the setup. A variety of extensions was necessary to keep the loading cell out of the chamber (see Figure 15). Therefore, a significant thermal expansion took place during the measurement. This made a crosshead movement compensation necessary, to keep the load constant. Figure 16 shows the resulting load- time and load-displacement curve. The compensation was realized

by a cyclic adjusting of the crosshead. This can be seen at the right picture of Figure 16, where the load stayed constant, and the crosshead was slightly moving.

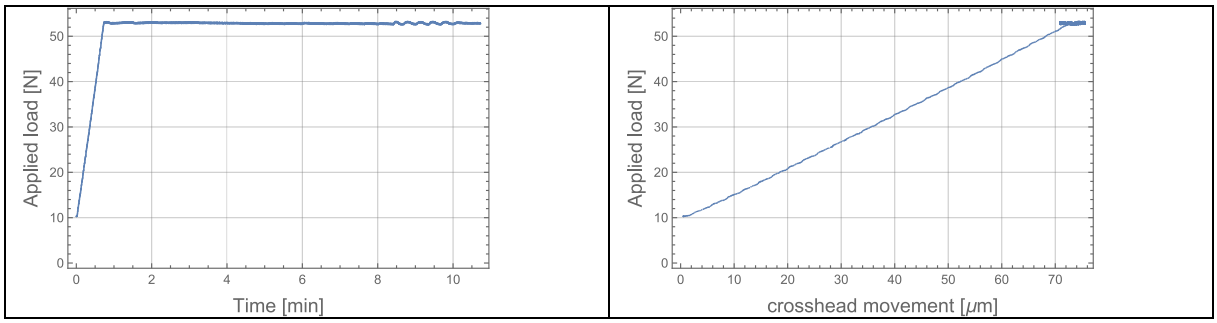

Figure 16: Load time curve and load-displacement curve measured at test at elevated temperature.

4.4. Combination of elevated humidity and temperature

The sealable bag was placed around the platens within the temperature chamber, to create a humid environment within the chamber. The saturated sodium chloride solution was placed together with the B3B testing fixture on the platen within the bag. (Figure 17)

Figure 17: B3B testing setup for testing at elevated temperature and elevated humidity.

The crosshead also had to be adjusted for this test setup to keep the load constant. The temperature and humidity were both measured with the microcontroller and recorded with a Python script.

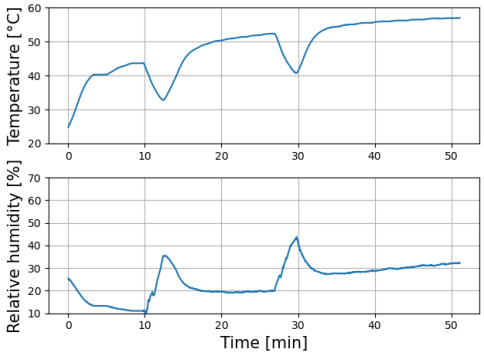

Figure 18: Temperature and humidity data during test measurement

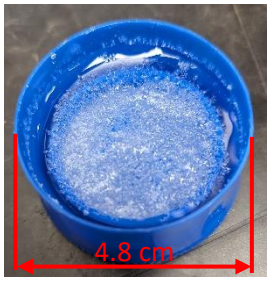

Figure 19: Crystallization of the NaCl-solution

As it is shown in Figure 18 the humidity settled way slower than the setup without the temperature chamber. It was detected that at the surface of the sodium chloride solution crystallization started and therefore the evaporation process was slowed down. Figure 19 shows the NaCl container after the measurement. That was probably due to the fast evaporation process at the beginning of the measurement caused by the especially hot temperature of the metal plate where the container was standing and the close distance between the fan and the solution surface. A way to reduce this issue was avoiding the direct contact between the container and the metal plate by putting a polymer disc in between and tilting the fan to reduce the air flow.

After these measures, the relative humidity had still not reached the expected value of 70 % RH. The humidity could be increased just by switching off the temperature chamber during the measurement. By keeping the door closed, the cooling process could be slowed down.

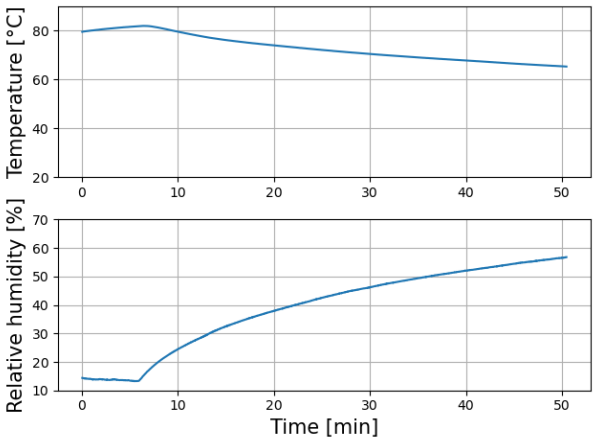

Figure 20: Temperature and humidity data during measurement at elevated temperature and humidity.

Figure 20 shows the temperature and humidity curve during a measurement. After turning off the temperature chamber, the relative humidity started rising. The measurement was started before the humidity was reached to reduce the temperature loss.

4.5. Dynamic measurement

To ensure that the ball on three balls fixture is capable for dynamic measurements at first a low frequency low cycle measurement was performed with the pressing machine itself. The frequency was kept low in order not to damage the actuation mechanism of the pressing machine. The routine for this measurement was implemented in the software of the pressing machine. By reversing the crosshead direction after reaching a specific maximum or minimum load, a triangular load signal was created.

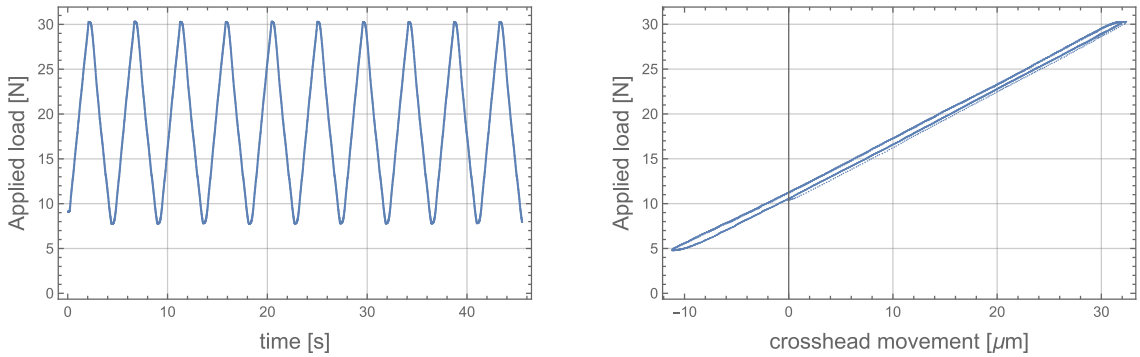

Figure 21: Load-time curve and load-displacement curve during dynamic test measurement.

Figure 21 shows the load-time and the load-displacement curve. Due to the load control of the program, a constant load amplitude could be ensured during the entire measurement. A small hysteresis can be seen on the load-displacement curve, but it does not move between the cycles, which suggests that the balls remain in their position.

A test setup with a piezoelectric actuator was considered to enable a higher number of cycles and a higher frequency. Due to the low maximum displacement of these actuators, the stiffness of the setup had to be estimated to determine the maximum possible load for a particular actuator. The load cell of the pressing machine had a maximum acquisition rate of 500 Hz, which also makes it usable for dynamic measurements. To obtain an estimate of the required displacement, the stiffness of the sample itself, the load frame (Figure 22) and the load frame with the temperature chamber (Figure 23) were determined.

Figure 22: Test setup at ambient conditions

Figure 23: Test setup for elevated temperature

To measure the stiffness of the specimen, a video extensometer (MTS Advantage Video extensometer) was used to track the movement of the top plate. The stiffness of the upper balls was considered negligible compared to the stiffness of the specimen, allowing the stiffness of the specimen to be determined directly.

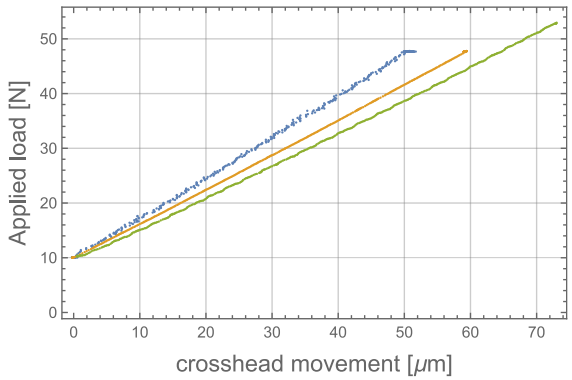

Test name	stiffness [N/μm]
Sample	0.75
System	0.64
System in temp chamber	0.60

Figure 24: Load-displacement curves for different setups and evaluated stiffness values.

Figure 24 shows the load-displacement curve of the different setups. The stiffness of the setups was calculated by determining the slope with a linear regression. The stiffness of the system without the temperature chamber is slightly lower than the stiffness of the specimen itself. It can also be seen that the additional extensions used on the setup for the temperature chamber reduce the stiffness even

further. Equation (19), Equation (1) and Hooke's law were combined in Equation (23) to calculate the necessary displacement for a specific strain.

$$\varepsilon = \frac{\sigma\,(1-\nu)}{E} = \frac{F\,f\,(1-\nu)}{E\,t^2} = \frac{k\,x\,f\,(1-\nu)}{E\,t^2} \tag{23}$$

where k is the stiffness, x is the displacement, f is the proportionality factor, ν is the Poisson's ratio of the material, E is the corresponding Young's modulus and t is the sample thickness.

By rearranging equation (23), the following formula for the displacement is obtained:

$$x = \frac{E\,t^2}{f\,(1-\nu)}\,\frac{\varepsilon}{k} \tag{24}$$

Table 4: Estimated displacement values for various strains for different setups

	Sample	System	System in Temp chamber
strain [%]	displacement [μm]	displacement [μm]	displacement [μm]
0.2	27.3	32.1	34.1
0.3	41.3	48.6	51.7
0.4	55.6	65.5	69.7
0.5	70.2	82.6	87.9
0.6	85.0	100.	106.
0.7	100.	118.	125.
0.8	115.	136.	144.
0.9	131.	154.	164.
1.	147.	173.	184.
1.1	163.	191.	204.
1.2	179.	211.	224.
1.3	196.	230.	245.
1.4	212.	250.	266.
1.5	230.	270.	287.

Table 4 shows the estimated displacement which is necessary to create a given strain with the different setups.

For the testing setup the piezoelectric actuator Kinetic Ceramics A100200 was considered. The actuator was powered with the amplifier Kinetic Ceramics KC1000-70-1. The actuator has a maximum displacement of 200 µm and a blocking force of 18 kN. This allows to apply strains of more than 1% at the testing system. Due to the high displacement and the high blocking force the actuator also has a high capacitance of 7.86 µF. This limited the maximal frequency to approximately 10 Hz because of the 70 mA current limit of the used amplifier.

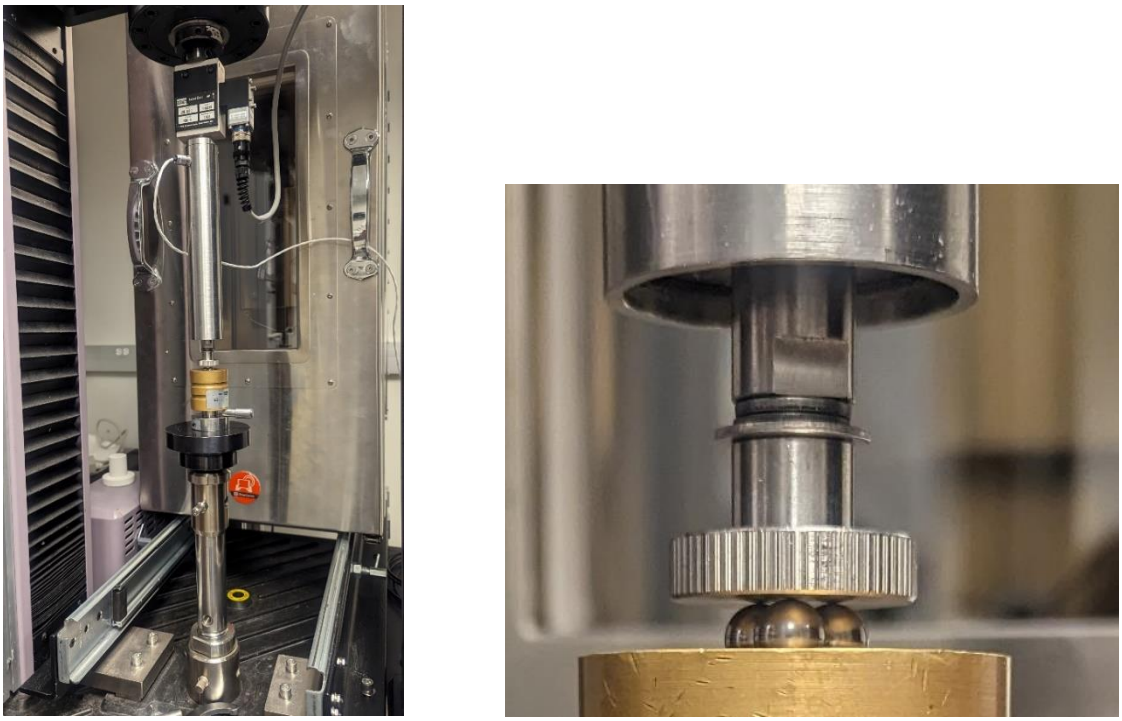

Figure 25: B3B-Testing setup for dynamic loading with the piezoelectric actuator.

With an adapter on the upper side and a thumb screw which acted as a punch on the bottom side, the piezoelectric actuator was attached to the testing setup. The signal for the actuator was generated by a waveform generator (Keyence 3390) and a DC power supply (Agilent E3612A) combined with a summing amplifier. This signal was connected to the piezo amplifier which generated a signal of up to 1000 V to get the full displacement.

To measure the force, the 1kN load cell of the testing machine was used. For this purpose, a program was implemented to measure the force over time without moving the crosshead.

5. Experiments and results for the moisture protection coatings

The moisture protection coating experiments were conducted on samples initially coated using thermal atomic layer deposition. The thermal silicon oxide layer was not removed. The ALD coating consisted of 15 nm Al_2O_3 and 5 nm TiO_2, both deposited at 200°C. A top layer of 2µm Parylene C was applied using chemical vapor deposition.

5.1. Static loading at elevated humidity experiments

The experiments under increased humidity were conducted at a relative humidity of 70%. For this purpose, equilibrium within the bag was waited for. A preload of 10 N was used. Three samples were tested. The mechanical stress was 0.9% strain for a duration of 30 minutes, corresponding to a force of 98.6 N. The temperature during the three measurements ranged between 23 - 24 °C. All samples were examined both before and after the mechanical stress using a Keyence VK-X3100 laser scanning microscope. Figure 26 shows the images of one of these samples, before and after the mechanical stress. The imprints visible at the edge of the sample were created by the handling of the samples with polymer tweezers. The center of the sample, which is the region of interest, was not affected by this.

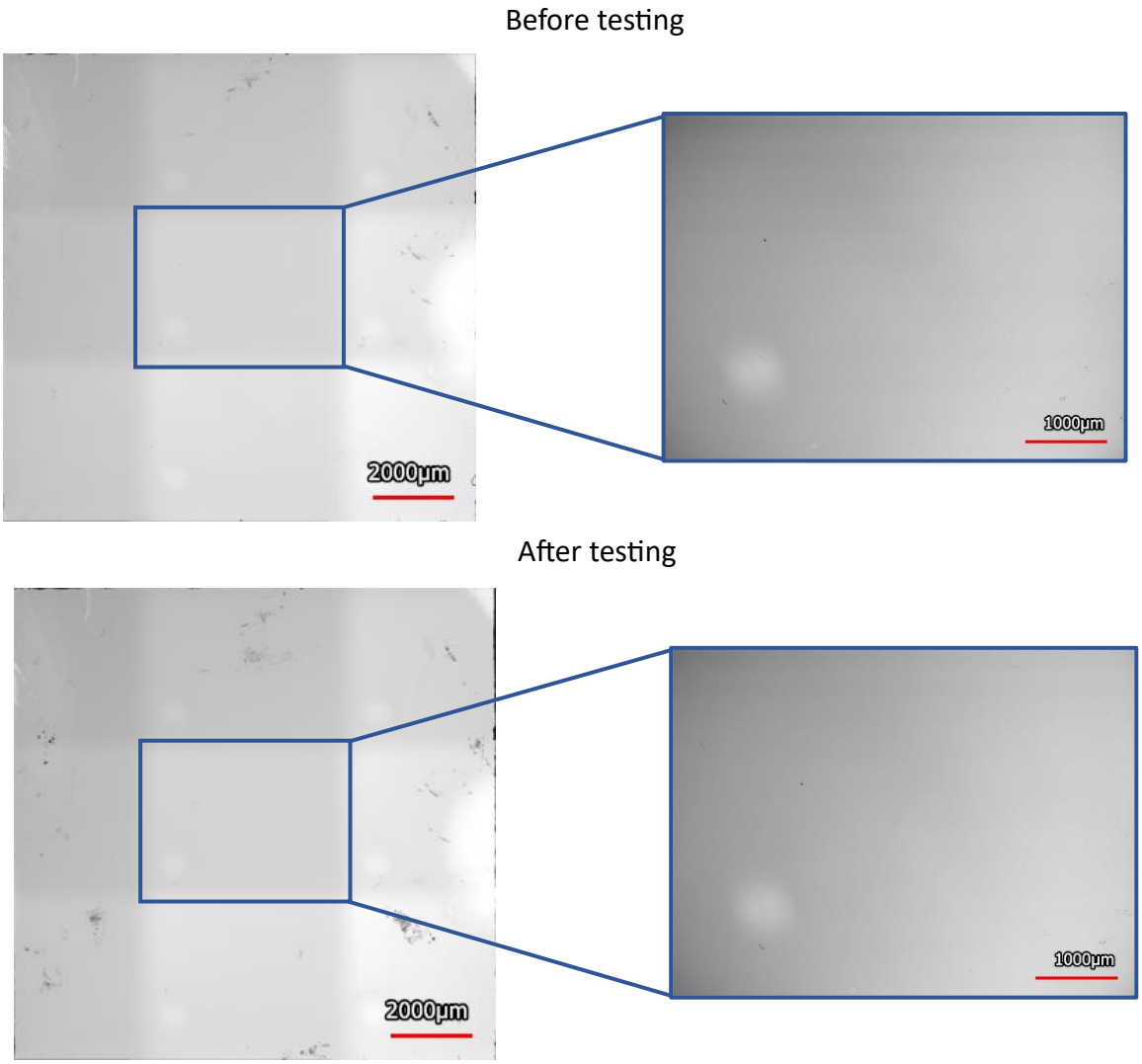

Figure 26: Laser scanning microscope images before and after static testing at elevated humidity.

With the laser scanning microscope, no cracks were detected in any of the samples. Additionally, the center of the samples was examined with circular differential interference contrast microscopy of a Zeiss AxioImager, as this is where the greatest mechanical stress occurred. Again, no cracks were detected. It can thus be concluded that the coating can withstand strains of up to 0.9% under increased humidity during static loading.

5.2. Static loading at elevated humidity and elevated temperature experiments

For the combination of increased humidity and elevated temperature, a temperature of 80 °C was targeted. Since the humidity did not increase during the operation of the temperature chamber's fan, it had to be deactivated during the measurement, resulting in a slight decrease in temperature. The mechanical stress was also set at 0.9% strain (equivalent to a force of 98.6 N) for a duration of 30 minutes. Under these conditions, two measurements were conducted.

In the first measurement, a temperature between 60 - 70°C was recorded. To avoid a further decrease in temperature, the measurement was conducted at a humidity between 50 - 65% RH. The humidity at the beginning of the measurement was 50% RH and reached 65% RH at the end. For the second measurement, the temperature of the temperature chamber was increased to 90 °C to ensure a measurement temperature between 70 - 80 °C. The humidity ranged from 40 - 55% RH. Laser scanning microscope images were also taken before and after the loading process. The images of the second measurement are shown in Figure 27.

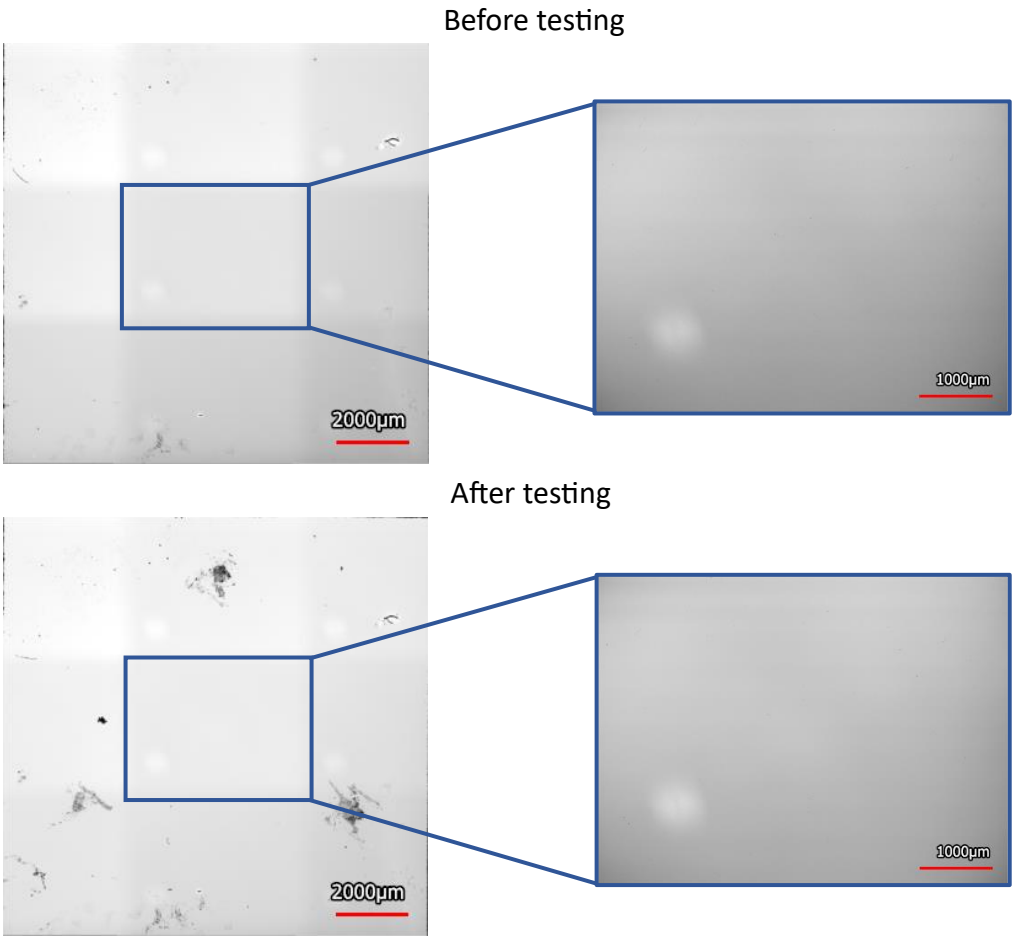

Figure 27: Laser scanning microscope images before and after static testing at elevated humidity and elevated temperature.

In this measurement, no cracks were detected either. The defects at the edge of the sample also resulted from handling. As in the previous case, the center was not affected. The samples were also investigated with C-DIC, without finding any cracks or defects.

5.3. Dynamic loading at ambient conditions

For the dynamic measurement, initially a voltage of 150 V was applied to avoid mechanical stress without electrical actuation. Subsequently, the crosshead was lowered to achieve a preload of 10 N. After removing the pin, a sinusoidal voltage between 150V and 700V was applied. A frequency of 5 Hz was chosen to not exceed the maximum current of the amplifier. The duration of the measurement was selected to reach approximately 10 000 cycles. Under these conditions, 3 samples were tested. Figure 28 shows the measured force over time for one of these samples. It can be observed that the force slightly decreased over time.

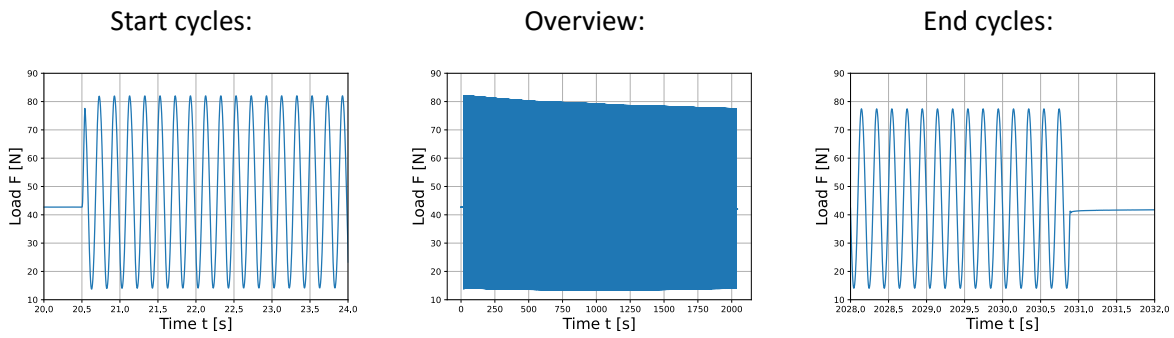

Figure 28: Load data over time of the dynamic measurement.

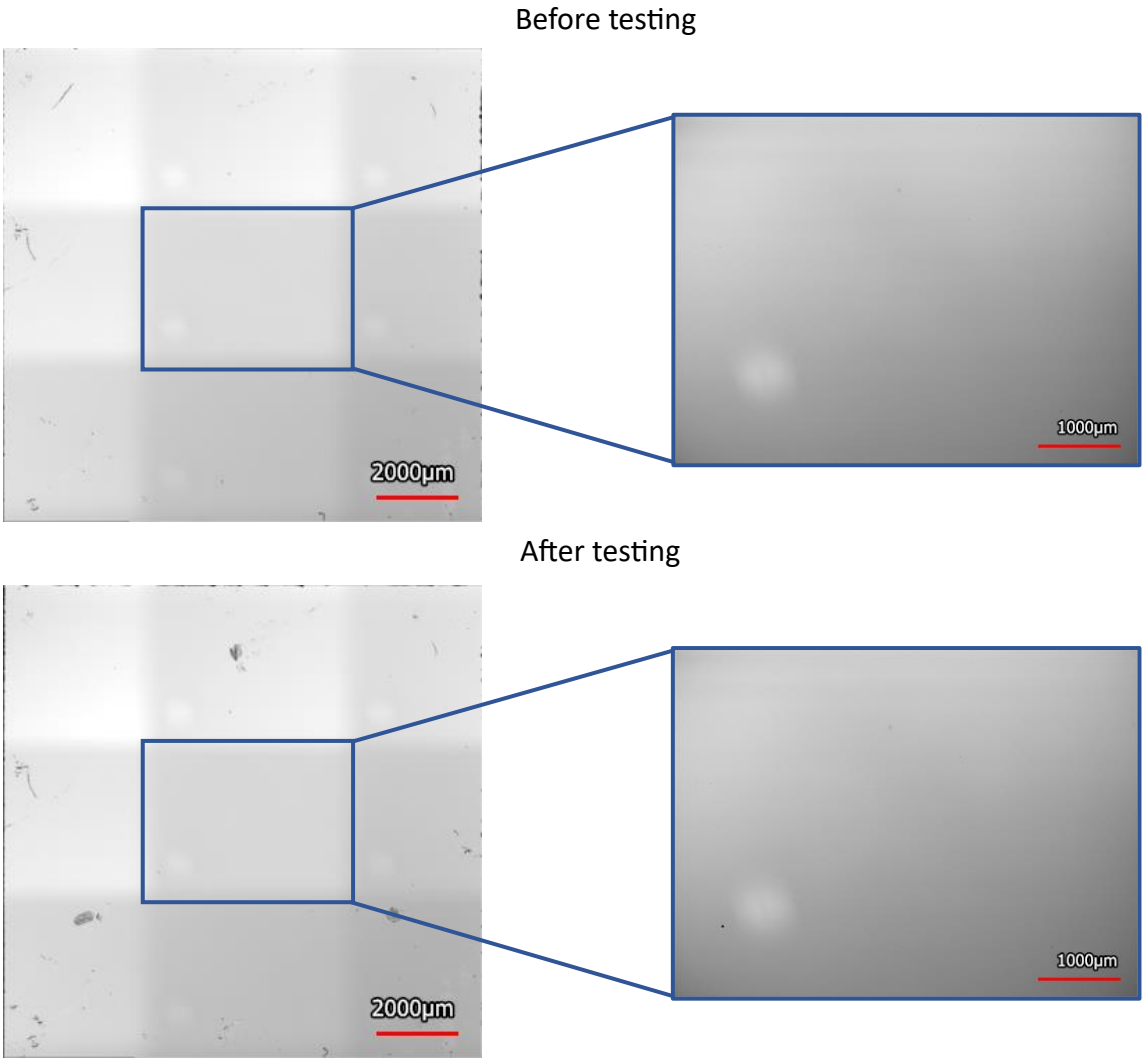

Figure 29: Laser scanning microscope images before and after dynamic testing at ambient conditions.

Figure 29 shows the corresponding laser scanning microscope images before and after the mechanical stress. The contact points of the balls are slightly more extended. This might indicate a slight movement of the balls along the sample, which could explain the slight decrease in force over time.

No cracks or defects were found in any of the three tested samples using the laser scanning microscope. Additionally, no defects were detected in the center of the sample using C-DIC of the optical microscope. Therefore, it can be inferred that the coating withstands dynamic loads under environmental conditions.

6. Establishing of the testing setups for the MLCCs

Two different experiments were considered for testing the MLCCs. Firstly, a miniaturized 3-point bending fixture was fabricated. This allowed for mechanical loading of the components. Additionally, a local thermal shock test was attempted, aiming to intentionally introduce defects through thermal stress.

6.1. MLCC samples

As samples, components from the manufacturer Knowles with the designation 1812J1000564KXB were used. These were 1812 multilayer ceramic capacitors with nickel barrier termination electrodes, a rated voltage of 100 V, and a nominal capacitance value of 560 nF. The dielectric material was X7R. The length of the components was 4.400 mm ±0.008 mm. The width in the body area was 3.039 mm ± 0.003 mm, and the thickness in the body area was 1.492 mm ± 0.021 mm. An exemplary image of the top view can be found in Figure 30.

Figure 30: Top view image of a MLCC sample.

6.2. Establishing the miniaturized 3-point bending setup

For the miniaturized 3-point bending fixture, a two-part bottom section consisting of an adapter block and a block containing the two support rollers, and a top section carrying the load roller were fabricated. The top section of the fixture was attached to the load cell using an adapter.

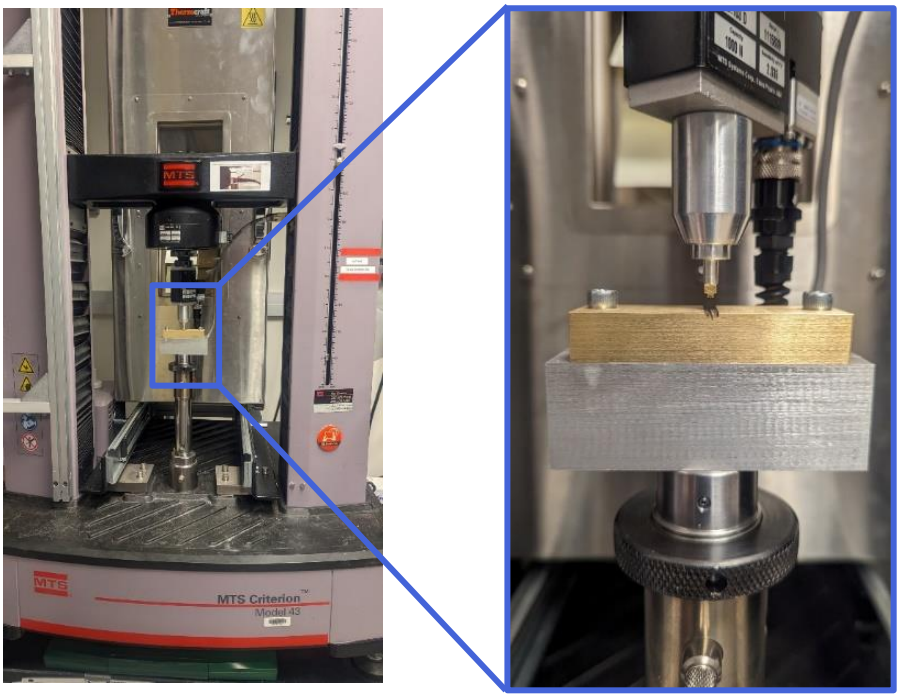

Figure 31: Miniaturized 3-Point-bending setup.

The upper part of the device was aligned with the groove between the support rollers and then fixed in place with superglue in order to align it correctly on the adapter. This is shown in Figure 32. On the underside, the adapter block was bolted to the extension of the testing machine.

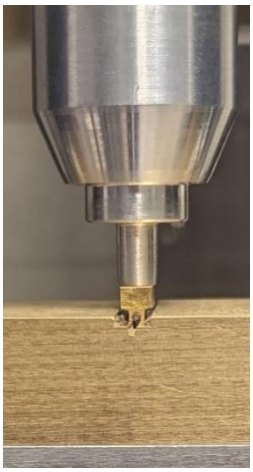

Figure 32: Image of the alignment procedure of the upper part of the 3-point-bending fixture.

6.3. Weibull analysis of the MLCCs

A Weibull analysis was performed to gain an understanding of the strength and probability of failure at a given stress level. For this purpose, 30 components were tested to failure. The Weibull analysis was performed using the Python library. This resulted in a characteristic strength of 204 MPa, with a corresponding 90% confidence interval of 199 - 209 MPa. The Weibull modulus was determined to be 13, with a confidence interval of 10 - 16. As a reference, a characteristic strength of 215 MPa with a Weibull modulus of 2.4 was used for comparison. The comparison components were slightly smaller (1206). The significant difference in the Weibull modulus could possibly be attributed to advances in manufacturing, resulting in a tighter distribution of defects. [19]

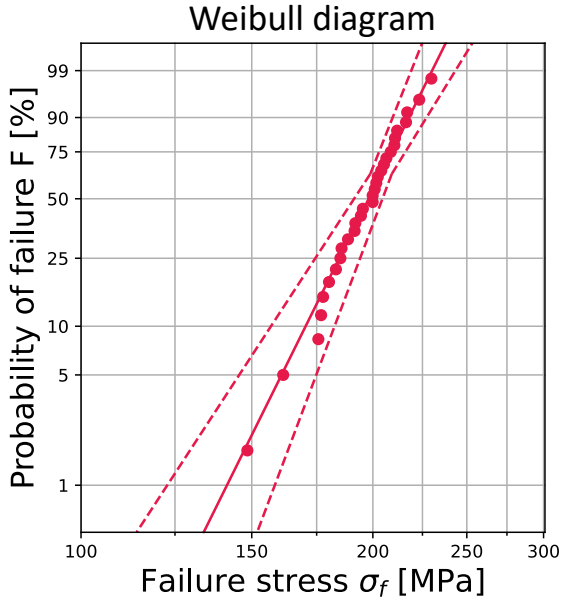

Figure 33: Weibull diagram of the MLCCs.

Using the Weibull analysis, an estimation of the probability of failure for various loads was subsequently done. For this purpose, equation (11) was used. The results are shown in Table 5.

Table 5: Failure estimation for different loads

F [%]	σ [MPa]	Load [N]
10	170	208
20	181	221
30	188	230
40	193	236
50	198	242
60	202	248
70	207	253
80	212	259
90	218	266

6.4. Local thermal shock experiments

In addition to the mechanical loading using the miniaturized 3-point bending test, a local thermal shock experiment was conducted. In this experiment, the sample was heated using a hot plate. A surface temperature of the hot plate of 310°C was measured. The sample was covered with a small ceramic crucible to reduce heat exchange with the surroundings. After approximately 30 minutes of waiting time, the thermal shock experiment was initiated. For this purpose, a cotton yarn piece was dipped in ice water. Afterwards, it was brought into contact with the center of the sample surface.

Figure 34: Image of the used hot plate for the local thermo-shock experiment

Figure 35: Image of the cotton yarn used for the local thermo-shock experiment

The samples were then both electrically characterized and examined using ultrasonic imaging. The experiment was conducted on 3 samples. No thermal shock damage was detected in any of the samples.

One possible reason for this could be the presence of compressive residual stress, especially in the center of the sample, which acts against the thermos-shock stress. [20]

Furthermore, it is assumed that the temperature at the center of the top surface of the sample is significantly lower than on the surface of the heating plate. To estimate this, a simplified simulation of the component, which did not take the inner electrodes into account, was conducted with Ansys 2023 R2. A heat transfer coefficient to the surroundings of 1000 W/(m^{2}K) was assumed. All other material parameters were taken from [19]. An image of the simulation is shown in Figure 36.

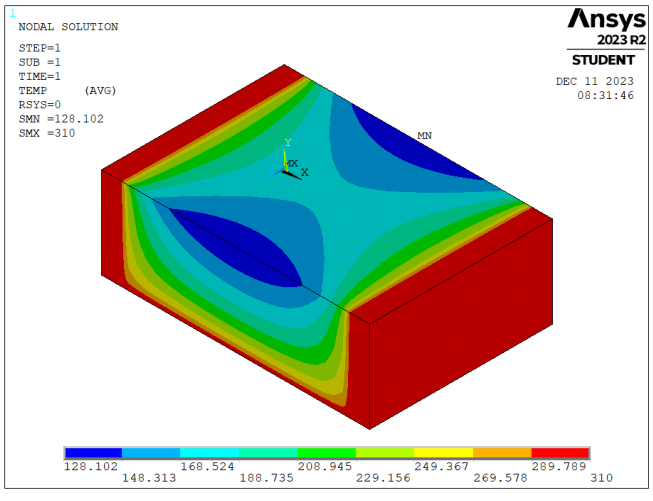

Figure 36: Image of the thermal simulation of the MLCC sample.

Additionally, the surface temperature of the component was measured using a thermocouple. The simulated temperature of approximately 170°C corresponded well with the measured temperature of 165°C. The ceramic shell, which was present over the sample during the heating process, was not considered in the simulation. It was observed that immediately after the removal of the shell, a temperature of 165°C was measured, and it did not change further. This may be attributed to the low heat capacity of the sample.

7. Experiments and results for the MLCCs

In the first experiment, the capacitance and loss factor of the samples were initially measured using a Stanford Research Systems Model SR715 LCR meter. Subsequently, they were subjected to mechanical loading. The duration of loading at maximum force was 30 seconds. For those samples that did not fail under mechanical loading, the capacitance and loss factor were measured again. The measured values are presented in Table 6. It was found that no significant differences in the electrical properties were observed before and after loading. Figure 37: Stereomicroscope image of tested samples after loading.

Table 6: Measurement results of mechanical loading of unpoled MLCC samples

Sample	Capacitance [nF]	Loss factor	Load [N]	Stress [MPa]	Capacitance [nF] (after loading)	Loss factor (after loading)
1	564	0.010	208	170	568	0.011
2	567	0.010	221	181	broke at loading	
3	567	0.010	221	181	574	0.012
4	570	0.010	221	181	broke at loading	

Figure 37 shows the respective samples under the stereomicroscope. It is evident that the support rollers caused slight indentation in the termination electrodes, but this did not affect the electrical properties.

Tensile side:

Compression side:

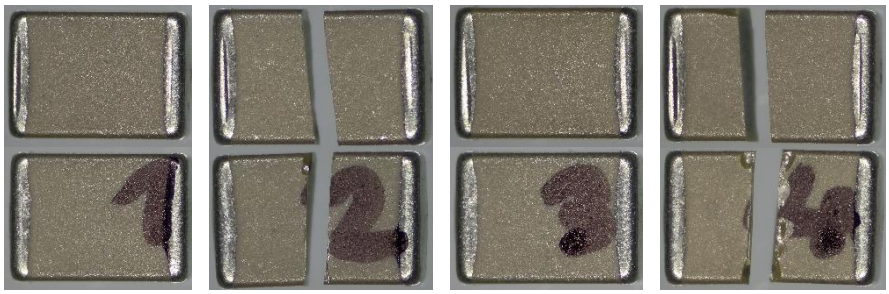

Figure 37: Stereomicroscope image of tested samples after loading.

For another experiment, 20 samples were polarized before mechanical loading to potentially amplify changes in the electrical properties. A voltage of 250V DC was applied for the polarization process. This corresponds to an electric field strength of approximately 100 kV/cm with a dielectric layer thickness of 25 µm (measured using the Zeiss AxioImager light microscope). The samples were polarized for a duration of 1 hour and then aged for 72 hours.

Table 7 displays the measured electrical properties before and after mechanical loading, as well as the applied loads and corresponding stresses. The electrical properties in this experiment were measured using the Keysight E4980A LCR meter. Samples not listed failed either during the polarization process or under mechanical loading. A loading duration of 60 seconds was chosen.

Table 7: Measurement results of mechanical loading of poled MLCC samples

Sample	Before poling		Load [N]	Stress [MPa]	After poling	
	C [nF]	Loss factor			C [nF]	Loss factor
2	545.3	0.0116	190	155	543.0	0.0117
3	567.3	0.0114	200	164	563.1	0.0121
4	554.9	0.0120	210	172	551.4	0.0121
6	546.2	0.0118	220	180	543.3	0.0116
8	532.8	0.0114	230	188	533.2	0.0119
14	546.7	0.0119	220	180	544.0	0.01 25
17	538.7	0.0113	220	180	536.0	0.0115
18	548.1	0.0135	220	180	544.4	0.0123

Although a slight reduction in capacitance and a slight increase in the loss factor D were observed, they were too small to be significant.

Thus far, no electrically measurable damage has been induced through mechanical loading.

8. Conclusion

The ball on three balls (B3B) experiment at elevated humidity and temperature has been established to mechanically characterize moisture barrier coatings. Measurements were conducted on a combination coating consisting of an inorganic ALD layer and an organic Parylene C layer. This coating was able to withstand both elevated humidity and the combination of humidity and increased temperature.

A setup for dynamic B3B measurements with a piezoelectric actuator has been established and tested. An experiment was conducted on the same coating, where again no cracks were observed in the coating after mechanical loading.

For the mechanical characterization of MLCCs, a 3-point bending test using a miniaturized support was established. A Weibull analysis was performed on commercial samples using this setup. With information on the strength distribution, attempts were made to load samples below the failure stress to introduce defects into the samples. No defects were detected through electrical characterization before and after loading. A local thermal shock experiment was conducted to explore another potential method for defect generation, but recognizable defects could not be produced.

A Python library has been implemented for Weibull analysis of the silicon substrate as well as for strength characterization of the MLCCs, enabling automatic evaluation of raw data. Subsequently, the determined Weibull parameters along with their 90% confidence intervals can be output and automatically visualized using Weibull diagrams and $m - \sigma_0$ diagrams.

Future work regarding moisture protection coatings could involve using an ultrasonic water vaporizer to ensure controlled humidity increase, even during operation of the temperature chamber, and testing multilayer coatings. As for the MLCCs, the already tested samples could be examined for possible defects using ultrasonic imaging. Furthermore, an experiment could be conducted with a B3B support. A testing fixture has already been fabricated for this purpose, for which suitable components would need to be procured.

9. References

[1] R. Dahl-Hansen, J. Polfus, E. Vollestad, B. Akkopru-Akgun, L. Denis, K. Coleman, F. Tyholdt, S. Trolier-McKinstry und T. Tybell, „Electrochemically driven degradation of chemical solution deposited ferroelectric thin-films in humid ambient," *J. Appl. Phys.,* Bd. 127, Nr. 24, p. 244101, 2020.

[2] S. Minnikanti, G. Diao, J. Pancrazio, X. Xie, L. Rieth, F. Solzbacher und N. Peixoto, „Lifetime assessment of atomic-layer-deposited Al2O3–Parylene C bilayer coating for neural interfaces using accelerated age testing and electrochemical characterization," *Acta Biomaterialia,* Bd. 10, pp. 960-967, 2014.

[3] C. Andersson, J. Ingmanb, E. Varescona und M. Kiviniemi, „Detection of cracks in multilayer ceramic capacitors by X-ray imaging," *Microelectron. Reliab. 64,* pp. 352-356, 2016.

[4] G. Hübschen, „Ultrasonic techniques for materials characterization," in *Materials Characterization Using Nondestructive Evaluation (NDE) Methods*, Elsevier, 2016, p. 177–224.

[5] A. Teverovsky, „Thermal-Shock Testing and Fracturing of MLCCs Under Manual-Soldering Conditions," *IEEE TRANSACTIONS ON DEVICE AND MATERIALS RELIABILITY,* Bd. 12, Nr. 2, pp. 413-419, 2012.

[6] A. Börger, P. Supancic und R. Danzer, „The ball on three balls test for strength testing of brittle discs: stress distribution in the disc," *J. Eur. Ceram. 22,* pp. 1425-1436, 2002.

[7] J. Kriegesmann, „Technische keramische Werkstoffe. Kapitel 6.2.3.1 - Der 4-Kugelversuch zur Ermittlung der biaxialen Biegefestigkeit spröder Werkstoffe. Unter Mitarbeit von Robert Danzer, Peter Supancic und Walter Harrer.," HvB Verlag GbR, Ellerau, 2009.

[8] M. Staudacher, T. Lube und P. Supancic, „The Ball-on-Three-Balls strength test for discs and plates: Extending and simplifying stress evaluation," *Journal of the European Ceramic Society,* Bd. 43, pp. 648-660, 2023.

[9] EN 843-1, „Hochleistungskeramik — Mechanische Eigenschaften monolithischer Keramik bei Raumtemperatur Teil 1: Bestimmung der Biegefestigkeit," Österreichisches Normungsinstitut, Wien, 2008.

[10] W. Weibull, „Statistical Theory of Strength of Materials," Royal Swedish Institute for Engineering Research, Stockholm, 1939.

[11] D. Munz und T. Fett, Ceramics Mechanical Properties, Failure Behaviour, Materials Selection, Heidelberg: Springer-Verlag, 1999.

[12] C1239 − 13 (2018), „Standard Practice for Reporting Uniaxial Strength Data and Estimating Weibull Distribution Parameters for Advanced Ceramics," ASTM International, West Conshohocken, 2018.

[13] M. Tanaka, K. Higashida, H. Nakashima, H. Takagi und M. Fujiwara, „Orientation dependence of fracture toughness measured by indentation methods and its relation to surface energy in single crystal silicon," *International Journal of Fracture,* Bd. 139, pp. 383-394, 2006.

[14] G. Janssen, M. Abdalla, F. van Keulen, B. Pujada und B. van Venrooy, „Celebrating the 100th anniversary of the Stoney equation for film stress: Developments from polycrystalline steel strips to single crystal silicon wafers," *Thin Solid Films,* Bd. 517, Nr. 6, pp. 1858-1867, 2009.

[15] K. Coleman, R. Bermejo, D. Leguillon und S. Trolier-McKinstry, „Thickness Dependence of crack initiation and propagation in stacks for piezoelectric microelectromechanical systems," *Acta Materialia,* Bd. 191, pp. 245-252, 2020.

[16] N. Dowling, Mechanical Behavior of Materials Engineering Methods for Deformation, Fracture and Fatigue, Edinburgh Gate: Pearson Education Limited, 2013.

[17] S. Wiederhorn, „Influence of Water Vapor on Crack Propagation in Soda-Lime Glass," *Journal of The American Ceramic Society Vol. 50, No. 8,* pp. 407-414, 11 May 1966.

[18] R. Bermejo, P. Supancic, C. Krautgasser, R. Morrell und R. Danzer, „Subcritical crack growth in Low Temperature Co-fired Ceramics," *Engineering Fracture Mechanics,* pp. 108-121, March 2013.

[19] R. Koripella, „Mechanical Behavior of Ceramic Capacitors," *IEEE TRANSACTIONS ON COMPONENTS, HYBRIDS, AND MANUFACTURING TECHNOLOGY,* Bd. 14, Nr. 4, pp. 718-724, 1991.

[20] G. Yang, Z. Yue, T. Sun, W. Jiang, X. Li und L. Li, „Evaluation of Residual Stress in a Multilayer Ceramic Capacitor and its Effect on Dielectric Behaviors Under Applied dc Bias Field," *J. Am. Ceram. Soc.,* Bd. 91, pp. 887-892, 2008.

[21] Y. Wang, W. Chu, Y. Su und L. Qiao, „Stress corrosion cracking of a PZT piezoelectric ceramics," *Mater. Lett. 57,* pp. 1156-1159, 2003.